Nuclear Science and Techniques (2026) 37:127
https://doi.org/10.1007/s41365-026-01926-1

Shielding integral experiment of slab Zr samples based on a D–T neutron source

Xin-Yi Pan[1] · Yang-Bo Nie[1] · Shi-Yu Zhang[1] · Yan-Yan Ding[1] · Qi Zhao[2,3] · Kuo-Zhi Xu[1] · Xiao-Yu Wang[1] · Bei-Bo He[1] · Hong-Tao Cheng[1] · Xi-Chao Ruan[1] · Jie Ren[1]

Received: 9 December 2024 / Revised: 30 December 2024 / Accepted: 24 January 2025 / Published online: 17 April 2026

Abstract

Zirconium (Zr) and its alloys are critical materials in nuclear reactors because of their low neutron absorption cross section, high-temperature stability, and excellent corrosion resistance. The accuracy and reliability of nuclear data evaluated for Zr isotopes are directly related to the safety and efficiency of nuclear engineering. To provide experimental data for refining Zr nuclear data, we obtained the leakage neutron time-of-flight (TOF) spectra of natural Zr samples with three thicknesses at six angles using the D–T fusion neutron source in an integral experimental setup. The experimental results were compared with simulated TOF spectra generated using the Monte Carlo N-Particle Transport Code and nuclear data libraries, including CENDL-3.2, ENDF/B-VIII.0, JEFF-3.3, and JENDL-5. An analysis of the calculated-to-experimental ratios revealed the following: (1) The CENDL-3.2 library lightly underestimated elastic scattering at small angles but significantly overestimated it at larger angles and in discrete inelastic scattering ranges. (2) The ENDF/B-VIII.0 library significantly underestimated the discrete inelastic scattering ranges. (3) The JEFF-3.3 library consistently overestimated the measurements in both the elastic and discrete inelastic scattering ranges. (4) The JENDL-5 library demonstrated the best agreement with the experimental data among all libraries. These results highlight the inconsistencies in existing nuclear data for Zr isotopes and emphasize the necessity for further refinement to enhance their accuracy and reliability.

Keywords Slab Zr · Leakage neutron spectra · Shielding integral experiment · Evaluated nuclear data

1 Introduction

Zirconium (Zr) has excellent nuclear properties, including a low thermal neutron absorption cross section (1.8×10^{-5} b), good high-temperature stability, and exceptional corrosion resistance [1–5]. Zr alloys can withstand harsh environments within nuclear reactors while minimizing neutron absorption, thereby enhancing the efficiency of nuclear reactions. Consequently, Zr alloys are commonly used in fuel cladding and cladding tubes. Additionally, Zr alloys are widely utilized as structural materials in other reactor components, such as pressure tubes, active area support structures, and nuclear fuel cores. These components play critical roles in the operation of nuclear reactors and must withstand extreme working conditions. With the continuous advancement of nuclear power technology and increasing global demand for clean energy, the prospects for the application of Zr in the nuclear industry are increasingly promising.

Before nuclear data can be effectively utilized, they must undergo integral validation testing to verify their accuracy and reliability. The fusion neutron integral experiment is a key method for validating nuclear data. By comparing the results obtained from these integral experimental measurements with those generated using Monte Carlo simulations,

This work was supported by the National Natural Science Foundation of China (Nos. 1177531, U2067205), the Research and Development Project of China National Nuclear Corporation (No. FD010241222552), and the Continuous-Support Basic Scientific Research Project (No. BJ010261223282).

✉ Yang-Bo Nie
nieyb@163.com

1 Key Laboratory of Nuclear Data, China Institute of Atomic Energy, Beijing 102413, China

2 School of Nuclear Science and Technology, Lanzhou University, Lanzhou 730000, China

3 Spallation Neutron Source Science Center, Dongguan 523803, China

we can assess the discrepancies between various nuclear data libraries. This comparison aids in identifying the limitations of each library, thereby providing valuable guidance to nuclear data developers for improving libraries [6–9].

Owing to the widespread application of Zr alloys in the nuclear industry, research on Zr-related nuclear data has been continuously conducted. Although numerous international differential experiments involving Zr have been performed, integral experimental measurements remain relatively scarce owing to the high cost of obtaining high-purity, large-sized Zr samples. Previous studies have included the measurement of leakage neutron spectra for spherical Zr samples irradiated by 14 MeV neutrons at Kyoto University [10], high-energy neutron scattering experiments conducted at the Rensselaer Polytechnic Institute [11], and integral experiments using a Cockcroft–Walton accelerator at the China Institute of Atomic Energy (CIAE) [12]. These studies revealed that simulation results based on the currently evaluated Zr data still exhibit discrepancies with experimental data. This highlights the necessity for further improvement of Zr isotope evaluation data. Conducting additional shielding integral experiments using Zr samples is essential to providing sufficient and high-quality data for refining Zr evaluated data.

In this study, Zr samples were irradiated with 14.5 MeV D–T neutrons, and the leakage neutron spectra were measured at six angles using the time-of-flight (TOF) method with an EJ-301 liquid scintillator detector. Monte Carlo simulations were subsequently performed using the Monte Carlo N-Particle Transport Code (MCNP) program [13, 14] to analyze Zr-related data from the CENDL-3.2 [15], ENDF/B-VIII.0 [16], JEFF-3.3 [17], and JENDL-5 [18] libraries. When 14.5 MeV neutrons interact with Zr samples, different reaction channels produce secondary neutrons of varying energies. These reaction channels include elastic scattering, discrete energy-level inelastic scattering, continuous energy-level inelastic scattering, and (n, 2n) reactions. Each of these channels primarily contributes to different time windows in the TOF spectra. A preliminary evaluation of the Zr-related data in different nuclear libraries was conducted by analyzing the calculated/experimental (C/E) deviations from various libraries and combining these with the cross-sectional information from each reaction channel.

Compared with earlier integral experiments involving Zr, this study extended the measurement of leakage neutron spectra to a wider range of angles, spanning from 47° to 133°, thereby providing a more comprehensive angular dataset. Furthermore, the measurements incorporated Zr samples of three different thicknesses, enabling the collection of more diverse and detailed experimental data. Additionally, this study validated the nuclear data of Zr from the latest release of China's Evaluated Nuclear Data Library (CENDL-3.2), enhancing the credibility and applicability of the dataset.

2 Experimental setup

The experiment was conducted using a 400-kV nanosecond-pulsed accelerator at CIAE. A shielding integral experimental setup, developed by the China Nuclear Data Center based on this accelerator, was utilized [19–25]. The experimental system included a T-Ti target, an associated particle detection system, samples, a shielding collimation system, and a monitoring system, all housed in a 20-m-long, 10-m-wide experimental hall with 2-m-thick heavy concrete walls. The main detector was placed in an adjacent hall to ensure that the neutrons leaking from the sample traveled more than 7 m before reaching the detector. This arrangement improved the neutron energy resolution and minimized background interference.

The beamline was positioned perpendicularly to the collimation line and maintained at an approximate height of 2 m. The experimental setup is shown in Fig. 1.

2.1 Neutron source

The 400-kV nanosecond-pulsed neutron generator [26] was used to produce pulsed neutrons for the experiment. The generator emits monoenergetic 14.5 MeV fast neutrons through the T(d, n)^{4}He reaction, achieved by bombarding a T-Ti target with a D$^+$ ion beam. The incident D$^+$ ion beam energy was 300 keV, with an average current of 20 μA, pulse width of 2 ns, and pulse frequency of 1.5 MHz. The T-Ti target, with an active zone diameter of 1.6cm and thickness of 1 mg/cm^2, generated a neutron yield of approximately 2×10^9 n/s.

2.2 Samples and measured angle

A standard polyethylene sample and three natural Zr (^{nat}Zr) slabs were used in the experiment. The dimensions of the polyethylene sample were $30cm \times 30cm \times 6cm$, and its density was 0.942 g/cm^3. The purity of the Zr sample reached 99.5%; detailed information is provided in Table 1.

Polyethylene was selected as the standard sample to validate the measurement system because of its well-characterized n-p elastic scattering cross section [27]. The interaction between neutrons and hydrogen involves only the elastic scattering reaction channel (n-p scattering), and the n-p scattering cross section is internationally recognized as a standard reference. By employing polyethylene, we could effectively validate the experimental system's reliability, including its data acquisition and processing capabilities before the measurements of the ^{nat}Zr samples.

Leakage neutron spectra were measured at six angles to ensure comprehensive data collection. For the 6-cm Zr

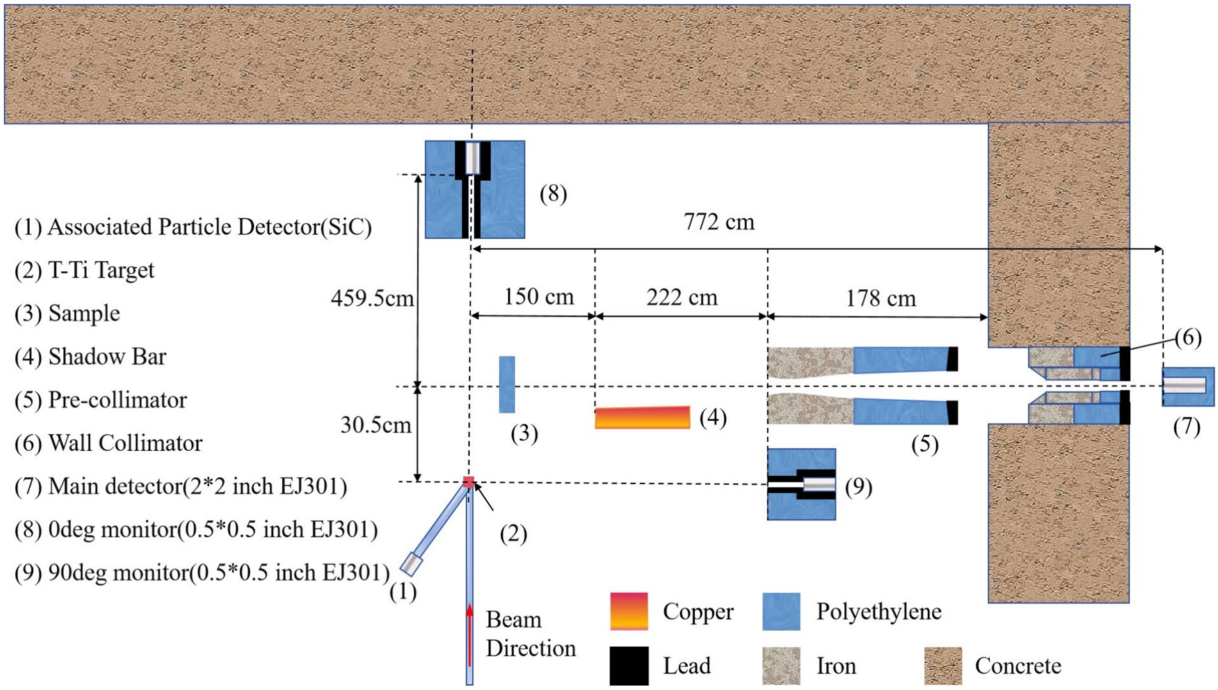

Fig. 1 (Color online) Experimental device layout diagram

Table 1 Details of samples

Sample	Size (cm^3)	Density (g/cm^3)	Major impurity (%)
^{nat}Zr_1	30 × 30 × 6	6.413	O (< 0.042); Hf (< 0.01)
^{nat}Zr_2	30 × 30 × 6	6.494	Fe (< 0.01); Cr (< 0.01)
^{nat}Zr_3	30 × 30 × 6	6.495	Cl (< 0.01)

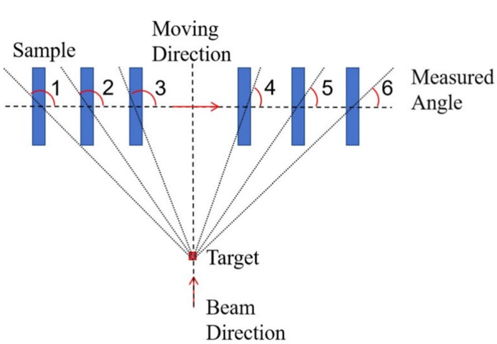

Fig. 2 (Color online) Measured angle and Zr sample movement

sample, measurements were conducted at 47°, 61°, 79°, 101°, 119°, and 133°. For the 12 and 18-cm samples, the angles were adjusted to 47°, 58°, 73°, 107°, 122°, and 133° to minimize interference with the monitoring system. The measurements were performed at different angles using an electric platform for precise sample positioning, as illustrated in Fig. 2.

2.3 Shield and collimator

The shielding and collimation system was designed to minimize the scattered neutron background and ensure the accuracy of the measured data [28]. It consists of three main components: a shadow bar, pre-collimator, and wall collimator. The shadow bar, positioned between the neutron source and pre-collimator, blocks direct neutron interactions with the pre-collimator material, preventing the generation of secondary neutrons. The wall and pre-collimators have a three-layer structure, as summarized below:

- **First layer (iron):** Reduces fast neutron energy via inelastic scattering.
- **Second layer (polyethylene):** Further reduces neutron energy to the thermal range through elastic scattering.
- **Third layer (lead):** Absorbs gamma rays generated during neutron interactions.

This system ensures that only neutrons scattered from the sample within the detector's solid angle reach the main detector, whereas background neutrons and gamma rays are effectively suppressed.

2.4 Detector systems and data acquisition

The experimental setup included an EJ-301 liquid scintillator as the primary detector, two monitor detectors, and an associated particle detector. The EJ-301 detector (diameter: 5.08 cm, thickness: 5.08 cm) measured the leakage neutrons emitted from the sample. Two monitor detectors (diameter: 1.27 cm, thickness: 1.27 cm), respectively, positioned at 0° and 90° relative to the beam direction, primarily measured the TOF spectra of the source neutrons. An associated particle detector based on a SiC detector was positioned at 135° to the beam direction to measure alpha particles and protons for neutron yield normalization [29–32].

The neutron yields were calculated using the following relationships:

$$N_n = K_\alpha \times N_\alpha, \quad N_n = K_p \times N_p, \tag{1}$$

where N_n is the neutron yield, N_α is the alpha particle count, and N_p is the proton count. K_α and K_p are the corresponding normalization coefficients, derived from the relationship between the neutron flux and alpha particle (or proton) flux in the unit solid angle at 135°. These calculations provide critical inputs for normalizing the experimental results.

The data acquisition system employed was GDDAQ [33], which uses Pixie-16 modules for digital signal processing. The key parameters of the Pixie-16 card are listed in Table 2. The system efficiently handled data collection, enabling the integration of TOF and pulse shape discrimination (PSD) analyses during post-processing.

Figure 3 illustrates the TOF measurement system. The pickup signal generated by the D^+ ion beam as it passed through a copper ring inside the tube in front of the target was sent to an acquisition card through a fast pre-amplifier. The signals from the three liquid scintillator detectors and beam pickup signal were processed together to calculate the neutron TOF.

Table 2 Specifications of the Pixie-16 data acquisition module

Parameter	Specification
Structure	6U PXI/PXIe
Number of channels	16
Sampling frequency (MHz)	500
Resolution (bit)	12
Maximum waveform capture duration (μs)	20
Data transmission rate (GB/s)	1

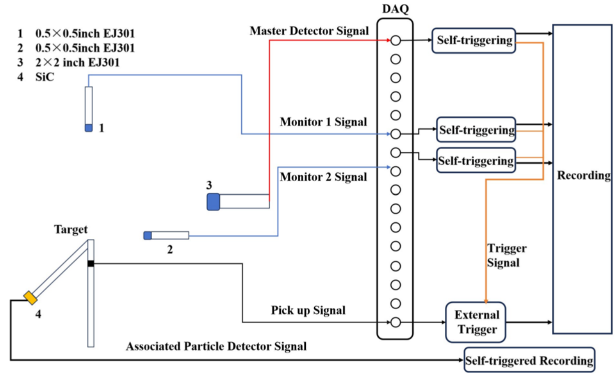

Fig. 3 (Color online) TOF measurement electronics system

2.5 Experimental methods and data processing

2.5.1 Inverse TOF method

The inverse TOF method was adopted to optimize measurement efficiency and reduce the dead time of the system. In this approach, the detector signal was used as the start signal and the beam pickup signal served as the stop signal. This method mitigated two major problems:

1. It avoided excessive data load on the acquisition system caused by the high-frequency (1.5 MHz) beam pickup signal.
2. It reduced system dead time resulting from the low-probability event of neutron detection, which often left start signals without corresponding stop signals.

The resulting inverse TOF spectrum was inverted during data processing to obtain the true TOF spectrum.

2.5.2 Data processing

Energy calibration of the EJ-301 detector was performed using standard gamma sources to ensure energy linearity and to set the measurement thresholds, which were essential for excluding noise signals. Gamma rays were inevitably produced during the interactions of neutrons with matter. The PSD method was employed to distinguish neutron signals from gamma signals by leveraging the differences in their pulse shapes.

A baseline correction was applied to each signal to reduce noise. The PSD value was calculated as the ratio of the slow component integral to the total signal integral. This enabled the effective separation of the neutron signals from the gamma signals. The impact of PSD on TOF spectra is shown in Fig. 4, where improved neutron spectra are evident after eliminating the gamma-ray signals.

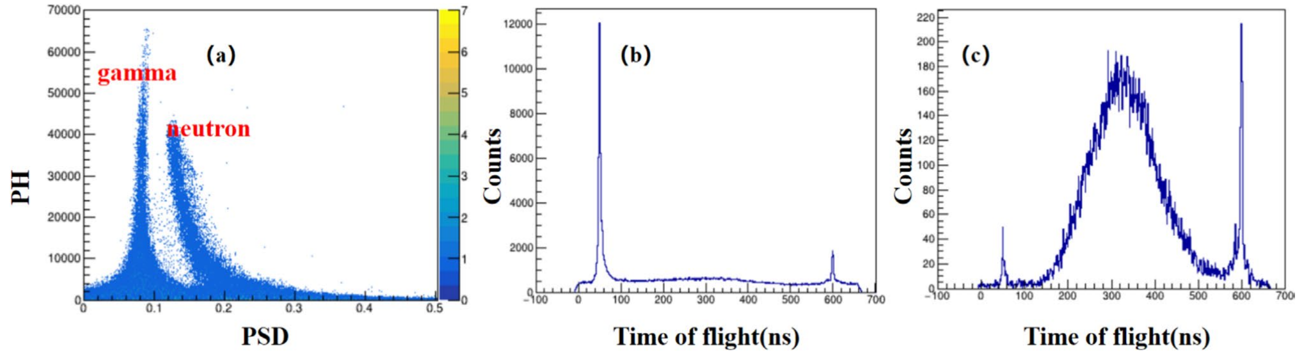

Fig. 4 (Color online) PSD discrimination results. (a) PH-PSD two-dimensional spectrum. (b) TOF spectrum of leakage neutrons before PSD discrimination. (c) TOF spectrum of leakage neutrons after PSD discrimination

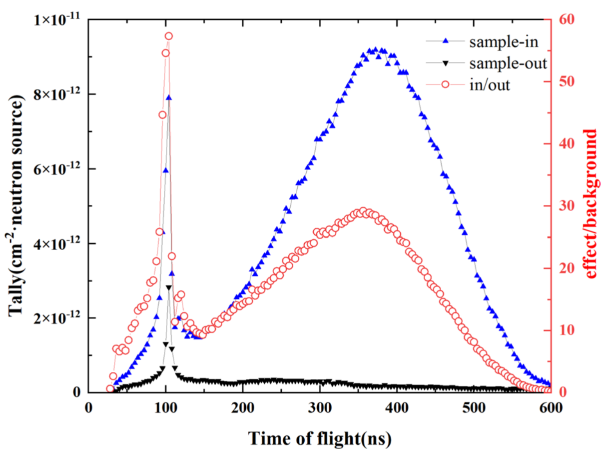

Fig. 5 (Color online) Measured leakage neutron time-of-flight spectra, illustrating a comparison between the effect and background spectra

During the experiment, the source neutrons not only interacted with the sample but also scattered with the air and surrounding structural materials. Because the measured leakage neutron spectrum specifically represents neutrons emitted from the sample after interactions with the source neutrons, the contributions from neutrons scattered by air and other materials had to be eliminated. To achieve this, we performed background measurements with the D–T neutron source present but without the sample. The resulting background spectrum was subsequently compared with the effect spectrum obtained when the sample was in place. The results are shown in Fig. 5, where "sample-in" denotes the effect spectrum measured with the sample, and "sample-out" represents the background spectrum measured without the sample. The effect-to-background ratio reached a peak value of 28 with an integrated effect-to-background ratio of 15 across the entire TOF spectrum.

3 Monte Carlo simulation

Shielding integral experiments validate nuclear data by comparing experimentally measured leakage neutron spectra with simulation results based on the evaluated nuclear data libraries. Accurate simulations are critical to the success of these experiments because discrepancies between the simulation and experimental results directly indicate areas for improvement in nuclear data evaluations. Among the various Monte Carlo simulation programs, MCNP is widely recognized for its advantages in data acquisition, material description, and geometric modeling.

MCNP simulations for shielding integral experiments involve detailed descriptions of the experimental setup, including the geometry, material composition, source neutron parameters, and detector response functions. The TARGET program [34] was employed to calculate the angular distribution of the source neutron energy spectrum, and the NEFF program [35] was used to determine the detection efficiency curves. The pulse time distribution of the source neutrons was derived by inverting the TOF spectrum measured using the monitor [36, 37]. These comprehensive inputs ensured that the simulations closely replicated the experimental conditions, thereby providing a reliable basis for comparison.

3.1 Geometric model

Accurate geometric modeling is essential for reliable simulations. Ideally, a detailed model that includes all the experimental structures would produce the most accurate results. However, such models significantly increase the computation time. To balance accuracy and efficiency, it is necessary to remove structures that have minimal impact on the simulation results. This was achieved through a series of simulations.

First, a detailed geometric model of the experimental hall and measurement system was created based on actual dimensions and materials. The leakage neutron spectrum of the polyethylene sample was calculated and used as the reference spectrum in this study. Subsequently, a weighting method was applied to obtain leakage neutron spectra of various sections of the experimental hall. These sections included the front, rear, left, and right walls (with the beam direction as the reference) as well as the ceiling and floor. In these simulations, wall weights were set to zero. Six spectra were generated and compared with the reference spectrum. Finally, the ratios of the studied spectra to the reference spectrum were calculated. The results are shown in Fig. 6(a). This enabled us to analyze the influence of different wall sections on the leakage neutron spectrum. Analysis of the ratios revealed that the ceiling, floor, front, and rear walls had minimal impact on the leakage neutron spectrum, with deviations from the reference spectrum of less than 0.1%. The left-side wall primarily influenced the low-energy region of the leakage neutron spectrum, whereas the right-side wall primarily affected the high-energy region.

To further investigate the effects of the left- and right-side walls, we divided them into different regions along the central axis of the collimated beam. With the weighting method again, the results showed that only the region within a 75 cm radius from the central axis of the side walls had a significant effect on the simulation results, as shown in Fig. 6(b) and (c).

In summary, except for the regions of the left- and right-side walls within a radius of 0.75 cm, the influence of the other hall walls on the leakage neutron spectrum can be neglected. These walls were excluded from the calculation model. The model considers only the geometric structure along the neutron path to the detector, which includes the target, sample, shadow bar, pre-collimator, wall collimator, and parts of the left and right walls. A schematic of the simplified model is shown in Fig. 7. The geometric model was constructed using the experimentally measured dimensions and material properties of the target, collimation components, and shielding walls. This approach ensured that the simulation results closely matched the experimental setup, thereby minimizing the discrepancies caused by geometric inaccuracies.

3.2 Source neutron parameters

The source neutron parameters, including the energy-angle distribution and pulse time distribution, play crucial roles in simulations. Accurate descriptions of these parameters are vital to ensuring consistency between simulated and experimental leakage neutron spectra. Any deviations in their description can lead to significant discrepancies.

In experiments using a D–T neutron source, not all incident D^+ ions react with the tritium in the target. Unreacted D^+ ions are deposited on the target, leading to subsequent D-D reactions. Over time, as the tritium in the target is depleted and more D^+ ions accumulate, the neutron source becomes a mixed field of D–T and D–D neutrons with dynamically changing yields. The energy-angle distributions of the D–T and D–D neutrons were calculated using the TARGET program, which incorporates the geometry and material parameters of the target. The ratios of the D–T and D–D neutron yields were determined from the measured alpha particle and proton ratios obtained from the associated particle detectors. These distributions were combined to produce source neutron spectra that accurately reflected the experimental conditions.

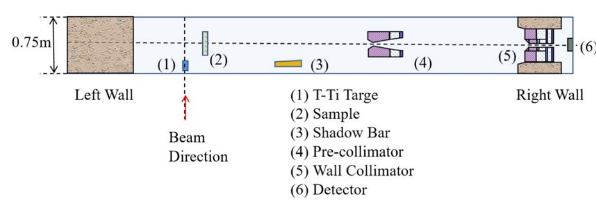

Fig. 7 (Color online) Schematic diagram of the calculation model for the shielding integral experiment measurement system

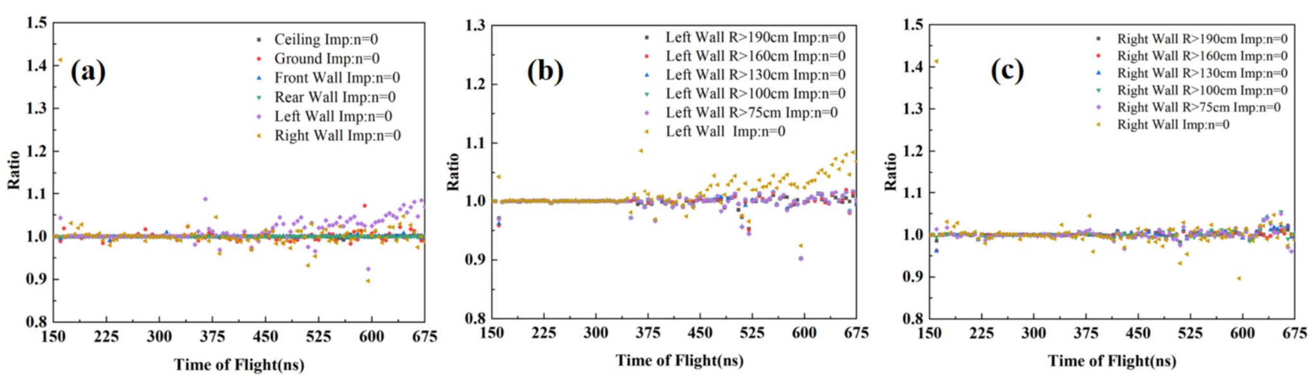

Fig. 6 (Color online) Ratio of the study spectra under different wall conditions to the reference spectra

The pulse time distribution of source neutrons was influenced by beam dynamics, such as initial energy dispersion, high-voltage ripple during acceleration, and deviations caused by beam clustering. These factors introduced slight changes in the source neutron emission profile over time. The TOF spectrum of the source neutrons, measured by the monitor, was combined with the simulated response matrices to calculate the pulse time distribution through inverse convolution, as shown in Eq. (2).

$$\begin{bmatrix} N_1 \\ N_2 \\ N_3 \\ \vdots \\ N_i \end{bmatrix} = \begin{bmatrix} R_{11} & R_{12} & R_{13} & \cdots & R_{1j} \\ R_{21} & R_{22} & R_{23} & \cdots & R_{2j} \\ R_{31} & R_{32} & R_{33} & \cdots & R_{3j} \\ \vdots & \vdots & \vdots & \ddots & \vdots \\ R_{i1} & R_{i2} & R_{i3} & \cdots & R_{ij} \end{bmatrix} \cdot \begin{bmatrix} \Phi_1 \\ \Phi_2 \\ \Phi_3 \\ \vdots \\ \Phi_j \end{bmatrix} \tag{2}$$

where N_i represents the measured TOF spectrum, $\boldsymbol{R}$ is the response matrix (with elements R_{ij}), and Φ_j is the pulse time distribution. This approach provided a precise representation of the source neutron emission profile for subsequent simulations.

3.3 Detector efficiency curve

The energy distribution of the neutrons leaking from the sample spans a broad range and requires a comprehensive understanding of the efficiency of the detector over this wide energy region. Because of the limited availability of monoenergetic neutron sources, experimentally measuring the detection efficiency across the entire energy spectrum is impractical. Instead, the NEFF program was used to calculate the efficiency curves based on the geometric parameters of the detector, photoresponse curve, and energy threshold. These calculated efficiency curves were validated against the available experimental data for similar systems, ensuring their reliability for TOF spectrum normalization.

3.4 Simulation of leakage neutron TOF spectrum

To evaluate the accuracy of Zr isotope data in various nuclear data libraries, we replaced the ^{nat}Zr material cards in the MCNP simulations. ^{nat}Zr consists of isotopes ^{90}Zr, ^{91}Zr, ^{92}Zr, ^{94}Zr, and ^{96}Zr, with proportions of 51.54%, 11.22%, 17.15%, 17.38%, and 2.8%, respectively. Evaluated nuclear data for these isotopes were sourced from the CENDL-3.2, ENDF/B-VIII.0, JEFF-3.3, and JENDL-5 libraries. The ENDF/B-VIII.0 library was used for all other materials, including Cu in the target structure, polyethylene, Fe, and Pb in the collimation system, etc. This ensured that any differences in the TOF spectra originated solely from ^{nat}Zr nuclear data.

After normalization using the calculated detector efficiency curves, the simulated TOF spectra were directly compared with the experimental results, providing insights into the accuracy of the nuclear data evaluations.

4 Results and discussion

4.1 Verification of the system using a standard sample

To ensure the reliability of the experimental measurement and data acquisition systems, we conducted a validation study by comparing the simulated and experimental results of the n-p scattering peaks using a polyethylene sample. The leakage neutron spectra from the polyethylene sample were experimentally measured at scattering angles of 47°, 61°, and 79°. The measured spectra were compared with the simulated results obtained using four evaluated nuclear data libraries: CENDL-3.2, ENDF/B-VIII.0, JEFF-3.3, and JENDL-5. The results are shown in Fig. 8. The close agreement between the experimental measurements and simulated results confirmed the accuracy and reliability of the

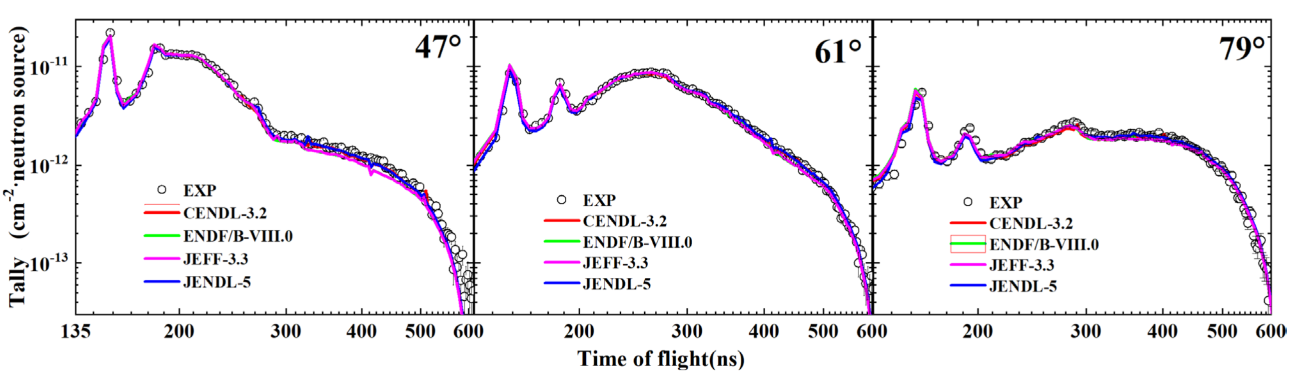

Fig. 8 (Color online) Comparisons of the measured and simulated leakage TOF spectra from the polyethylene sample

measurement system, data acquisition setup, and subsequent data processing procedures employed throughout the study.

4.2 Uncertainties analysis

The experimentally measured TOF spectrum of leaked neutrons must be normalized before it can be compared with simulation results; the normalized TOF spectrum is given by Eq. (3):

$$TOF_{\text{final}} = \frac{TOF_{\text{out}}}{N_{\text{n}} \times S} = \frac{TOF_{\text{in}} \times \epsilon_{\text{EN}}}{(K_{\alpha} \times N_{\alpha} + K_{\text{p}} \times N_{\text{p}}) \times S} \tag{3}$$

where

- TOF_{out} denotes the neutron TOF spectrum count detected by the detector, which is equal to the actual neutron TOF spectrum count TOF_{in} multiplied by the detector efficiency ϵ_{EN}.
- N_{n} denotes the source neutron count, which is equal to the detected alpha particle counts N_{α} and proton counts N_{p} multiplied by the corresponding coefficients K_{α} and K_{p}, and then summed.
- S represents the detector area.

Therefore, the main sources of error include the following:

- The statistical error of each time bin of the neutron TOF spectrum obtained from experimental measurements ($< 3\%$).
- The error of the associated particle monitoring system ($< 3\%$).
- The statistical error of the alpha particle counts and proton counts ($< 0.2\%$).
- The detector efficiency error ($< 3\%$).
- The stereoscopic angle error caused by the experimental samples and detector placement ($< 1\%$).

4.3 Measurement results of the Zr samples

The leakage neutron TOF spectra of $^{\text{nat}}$Zr samples with three thicknesses at six angles were measured in the experiment, resulting in 18 sets of data. The results for the three thicknesses are shown in Figs. 9, 10, and 11 for comparison with the leakage neutron spectra simulated by MCNP based on CENDL-3.2, ENDF/B-VIII.0, JEFF-3.3, and JENDL-5 libraries.

By comparing the calculated and experimental leakage neutron spectra, the following observations were made:

1. At approximately 156 ns, the simulation results of the CENDL-3.2 library slightly underestimated the experimental results at small angles (below 79°) but significantly overestimated them at large angles.

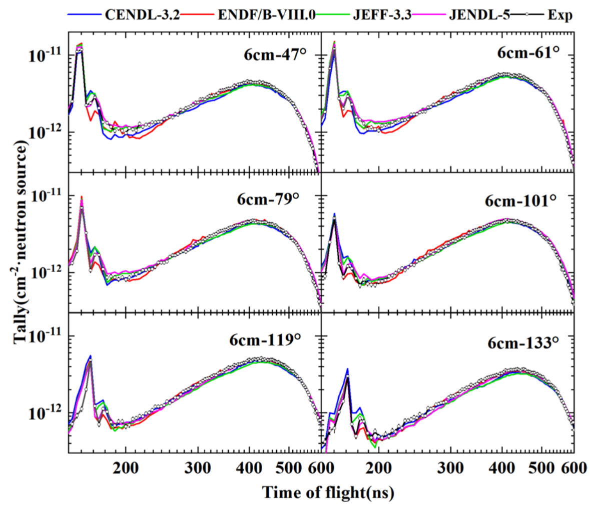

Fig. 9 (Color online) Comparison between calculated and measured leakage spectra of the 6 cm $^{\text{nat}}$Zr sample

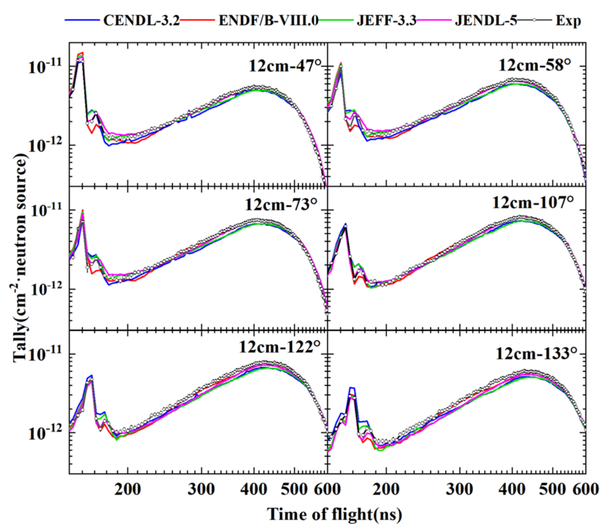

Fig. 10 (Color online) Comparison between calculated and measured leakage spectra of the 12 cm $^{\text{nat}}$Zr sample

2. At approximately 164 ns, the simulation results of CENDL-3.2 and JEFF-3.3 libraries were higher than the experimental results across all angles, whereas the simulation of ENDF/B-VIII.0 library was lower than the experimental results at small angles (47°, 58°, and 61°).

3. The simulation results for CENDL-3.2 and JEFF-3.3 libraries were lower than the experimental results for 300 ns–500 ns.

4.3.1 Change in C/E values with TOF

C/E values were obtained by dividing the simulation results from the CENDL-3.2 library by the experimental data. The

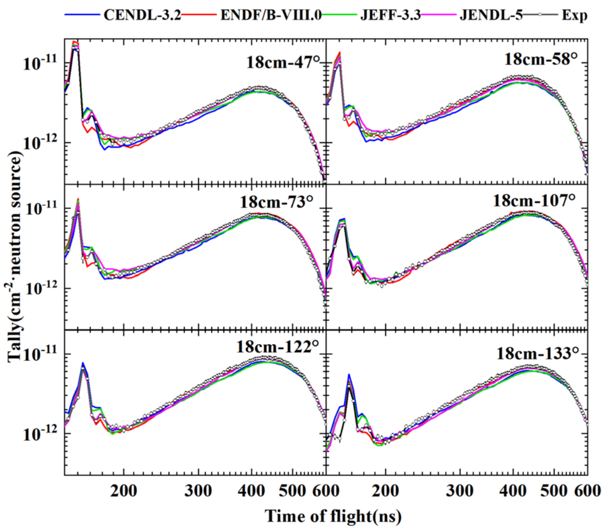

Fig. 11 (Color online) Comparison between calculated and measured leakage spectra of the 18 cm ^{nat}Zr sample

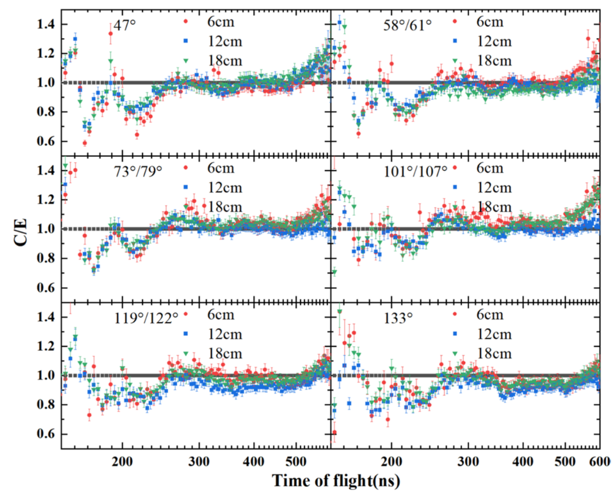

Fig. 13 (Color online) C/E values calculated from the simulation results of the ENDF/B-VIII.0 library

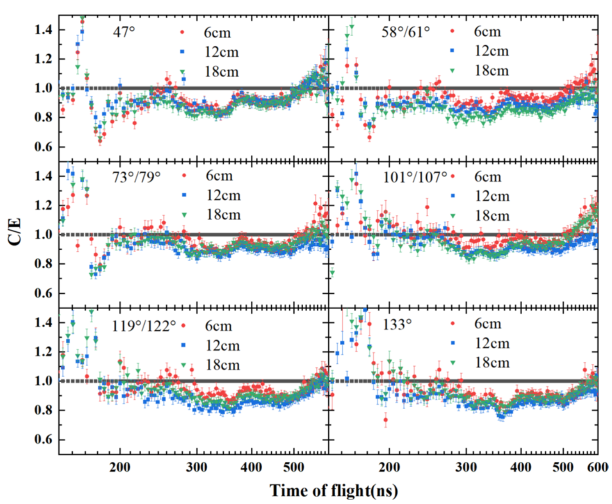

Fig. 12 (Color online) C/E values calculated from the simulation results of the CENDL-3.2 library

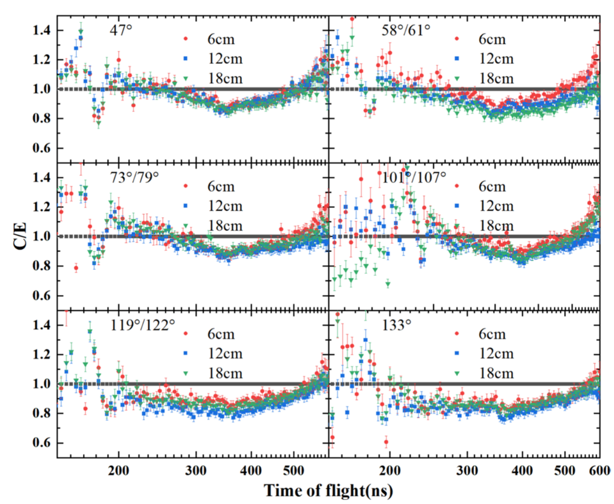

Fig. 14 (Color online) C/E values calculated from the simulation results of the JEFF−3.3 library

variation in C/E with TOF is shown in Fig. 12. As indicated, between 145 and 160 ns at small angles (47°, 58°, and 61°), the simulation results were slightly lower than the experimental values, whereas at larger angles, they were clearly higher. Near 164 ns, the simulation results exceeded the experimental values; however, between 250 and 550 ns, the simulation results were lower than the experimental values.

Similarly, C/E values were obtained by dividing the simulation results from the ENDF/B-VIII.0 library by the experimental data. The variation in C/E with TOF is shown in Fig. 13. As the figure shows, between 145 and 160 ns, the simulation results are higher than the experimental values; however, between 160 ns and 250 ns, most of the simulation results were lower than the experimental values.

For the JEFF-3.3, the variation in C/E with TOF is shown in Fig. 14. As shown, between 145 and 160 ns, the simulation results were higher than the experimental values, particularly at smaller angles ($\leq 79°$). Between 300 and 500 ns, the simulation results were lower than the experimental values, and this discrepancy was even more pronounced at larger angles.

For the JENDL-5 library, the variation in C/E with TOF is shown in Fig. 15. As shown, between 145 and 150 ns, at smaller angles ($< 101°$), the simulation results exceeded the experimental values. Between 220 and 400 ns, at larger angles ($> 119°$), the simulation results were lower than the experimental values.

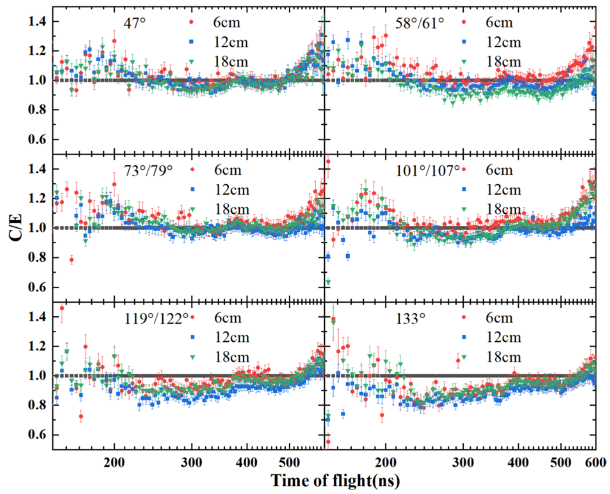

Fig. 15 (Color online) C/E values calculated from the simulation results of the JENDL-5 library

4.3.2 Comparison of C/E values in different energy regions

Discrepancies exist between simulations from different libraries and experimental results. These differences are caused by variations in the reaction cross sections related to secondary neutron production in each library. Analyzing these discrepancies can help identify potential limitations within libraries.

Using NDPlot [38] software developed by the China Nuclear Data Center, we obtained the secondary neutron energy spectra and energy spectra of different reaction channels produced by 14.5 MeV neutrons incident on ^{nat}Zr samples from the CENDL-3.2 library. The results, shown in Fig. 16, were derived by inputting the proton number, mass number of the target nucleus, and the energy of the incident particle.

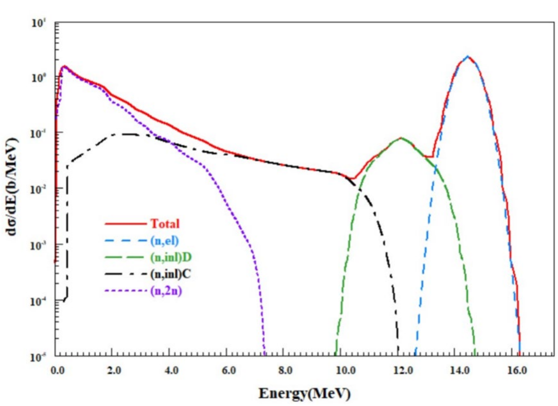

Fig. 16 (Color online) Secondary neutron energy spectrum produced by 14.5 MeV incident neutrons on ^{nat}Zr sample from the CENDL-3.2 library

According to the contribution of different reaction channels to the total cross section, the entire energy region can be divided into the following intervals:

- **Elastic scattering interval (n, el)**: $13.4 - 15MeV$.
- **Discrete energy-level inelastic scattering interval (n, inl)D**: $10.6 - 13.4MeV$.
- **Continuous energy-level inelastic scattering interval (n, inl)C**: $4.0 - 10.6MeV$.
- **(n, 2n) reaction interval**: $0.8 - 4.0MeV$.

These energy intervals correspond to TOF intervals at different angles, as listed in Table 3.

To analyze the cross-sectional data of different reaction channels, we calculated the C/E values for the measurements of samples with different thicknesses at different angles and compared them with the simulation results of CENDL-3.2, ENDF/B-VIII.0, JEFF-3.3, and JENDL-5 libraries, as shown in Table 4.

4.3.3 Variation in C/E values with angles

The variation in the C/E values with angle for different reaction channels of various thicknesses is illustrated in Fig. 17, from which the following can be observed.

1. In the elastic scattering energy range, the C/E values for ENDF/B-VIII.0, JEFF-3.3, and JENDL-5 libraries showed little variation with the angle. In contrast, the C/E values from the CENDL-3.2 library increased as the angle increased. Although initially lower than those of the other three databases at smaller angles (47°, 58°, 61°, and 73°), the C/E values of CENDL-3.2 library eventually surpassed those at larger angles.

2. In the discrete energy-level inelastic scattering energy range, the C/E values from the ENDF/B-VIII.0 library were noticeably lower than those from the other three libraries at all angles. Except for 122° and 133°, the C/E values of the

Table 3 TOF regions of each reaction channel at different angles

Angle (°)	(n, el) (ns)	(n, inl)D (ns)	(n, inl)C (ns)	(n, 2n) (ns)
47	147–155	155–173	173–277	277–610
58	147–156	156–174	174–279	279–616
61	148–156	156–174	174–280	280–618
73	148–157	157–175	175–282	282–623
79	149–157	157–176	176–283	283–626
101	151–159	159–178	178–287	287–635
107	152–160	160–179	179–288	288–638
119	154–162	162–182	182–292	292–644
122	154–163	163–182	182–293	293–646
133	157–166	166–185	185–297	297–654

Table 4 C/E value of each reaction channel for four libraries

Thickness–Angle	Reaction channel	CENDL-3.2	ENDF/B-VIII.0	JEFF-3.3	JENDL-5
6 cm–47°	(n, el)	0.923 ± 0.030	1.183 ± 0.039	1.152 ± 0.037	1.093 ± 0.036
	(n, inl)D	1.106 ± 0.038	0.764 ± 0.026	1.128 ± 0.038	1.040 ± 0.035
	(n, inl)C	0.902 ± 0.029	0.908 ± 0.029	0.998 ± 0.032	1.032 ± 0.033
	(n, 2n)	0.917 ± 0.029	0.980 ± 0.031	0.940 ± 0.030	1.002 ± 0.032
6 cm–61°	(n, el)	0.853 ± 0.028	1.217 ± 0.040	1.192 ± 0.039	1.107 ± 0.036
	(n, inl)D	1.208 ± 0.041	0.816 ± 0.028	1.199 ± 0.041	1.061 ± 0.036
	(n, inl)C	0.930 ± 0.030	0.944 ± 0.030	1.029 ± 0.030	1.075 ± 0.035
	(n, 2n)	0.933 ± 0.030	1.008 ± 0.032	0.950 ± 0.030	1.017 ± 0.032
6 cm–79°	(n, el)	1.243 ± 0.044	1.377 ± 0.048	1.275 ± 0.045	1.233 ± 0.043
	(n, inl)D	1.084 ± 0.038	0.820 ± 0.029	1.043 ± 0.037	0.986 ± 0.035
	(n, inl)C	0.980 ± 0.032	1.000 ± 0.032	1.020 ± 0.033	1.068 ± 0.035
	(n, 2n)	0.942 ± 0.030	1.039 ± 0.033	0.951 ± 0.030	1.026 ± 0.033
6 cm–101°	(n, el)	1.226 ± 0.044	1.178 ± 0.042	1.128 ± 0.040	1.064 ± 0.038
	(n, inl)D	1.254 ± 0.048	0.893 ± 0.034	1.240 ± 0.045	1.140 ± 0.043
	(n, inl)C	1.016 ± 0.033	1.036 ± 0.034	0.984 ± 0.032	1.022 ± 0.033
	(n, 2n)	0.969 ± 0.031	1.056 ± 0.033	0.968 ± 0.031	1.047 ± 0.033
6 cm–119°	(n, el)	1.394 ± 0.050	1.202 ± 0.043	1.113 ± 0.041	1.087 ± 0.039
	(n, inl)D	1.180 ± 0.044	0.826 ± 0.031	1.120 ± 0.042	0.964 ± 0.036
	(n, inl)C	0.984 ± 0.032	0.977 ± 0.032	0.911 ± 0.029	0.937 ± 0.030
	(n, 2n)	0.924 ± 0.029	0.991 ± 0.031	0.916 ± 0.029	0.988 ± 0.031
6 cm–133°	(n, el)	1.477 ± 0.057	1.188 ± 0.046	1.155 ± 0.045	1.100 ± 0.042
	(n, inl)D	1.327 ± 0.053	0.866 ± 0.035	1.135 ± 0.046	0.972 ± 0.039
	(n, inl)C	0.950 ± 0.031	0.953 ± 0.031	0.869 ± 0.028	0.884 ± 0.029
	(n, 2n)	0.900 ± 0.029	0.958 ± 0.030	0.896 ± 0.028	0.957 ± 0.030
12 cm–47°	(n, el)	0.965 ± 0.031	1.220 ± 0.040	1.147 ± 0.037	1.087 ± 0.035
	(n, inl)D	1.090 ± 0.038	0.822 ± 0.028	1.152 ± 0.040	1.090 ± 0.038
	(n, inl)C	0.917 ± 0.030	0.928 ± 0.030	0.990 ± 0.032	1.018 ± 0.033
	(n, 2n)	0.910 ± 0.029	0.997 ± 0.032	0.928 ± 0.029	0.989 ± 0.031
12 cm–58°	(n, el)	0.906 ± 0.030	1.215 ± 0.040	1.172 ± 0.039	1.096 ± 0.036
	(n, inl)D	1.180 ± 0.042	0.851 ± 0.030	1.204 ± 0.043	1.123 ± 0.040
	(n, inl)C	0.887 ± 0.029	0.929 ± 0.030	0.972 ± 0.031	1.006 ± 0.032
	(n, 2n)	0.883 ± 0.028	0.976 ± 0.031	0.899 ± 0.028	0.965 ± 0.031
12 cm–73°	(n, el)	0.972 ± 0.032	1.168 ± 0.039	1.132 ± 0.038	1.059 ± 0.035
	(n, inl)D	1.037 ± 0.036	0.774 ± 0.027	1.079 ± 0.038	1.037 ± 0.036
	(n, inl)C	0.931 ± 0.030	0.984 ± 0.032	1.004 ± 0.032	1.019 ± 0.033
	(n, 2n)	0.897 ± 0.028	0.997 ± 0.032	0.911 ± 0.029	0.981 ± 0.031
12 cm–107°	(n, el)	1.199 ± 0.041	1.130 ± 0.039	1.099 ± 0.038	1.018 ± 0.035
	(n, inl)D	1.109 ± 0.038	0.863 ± 0.030	1.109 ± 0.038	0.998 ± 0.034
	(n, inl)C	0.970 ± 0.031	0.995 ± 0.032	0.935 ± 0.030	0.965 ± 0.031
	(n, 2n)	0.904 ± 0.029	0.993 ± 0.031	0.905 ± 0.029	0.980 ± 0.031
12 cm–122°	(n, el)	1.178 ± 0.041	1.048 ± 0.036	1.016 ± 0.035	0.965 ± 0.033
	(n, inl)D	1.185 ± 0.043	0.875 ± 0.032	1.095 ± 0.040	0.988 ± 0.036
	(n, inl)C	0.893 ± 0.029	0.917 ± 0.029	0.839 ± 0.027	0.864 ± 0.028
	(n, 2n)	0.859 ± 0.027	0.931 ± 0.029	0.859 ± 0.027	0.925 ± 0.029
12 cm–133°	(n, el)	1.542 ± 0.057	1.258 ± 0.046	1.211 ± 0.045	1.138 ± 0.042
	(n, inl)D	1.222 ± 0.044	0.884 ± 0.033	1.135 ± 0.041	0.997 ± 0.036
	(n, inl)C	0.931 ± 0.030	0.956 ± 0.031	0.869 ± 0.028	0.883 ± 0.028
	(n, 2n)	0.885 ± 0.028	0.958 ± 0.030	0.883 ± 0.028	0.949 ± 0.028

Table 4 (continued)

Thickness–Angle	Reaction channel	CENDL-3.2	ENDF/B-VIII.0	JEFF-3.3	JENDL-5
18 cm–47°	(n, el)	0.958 ± 0.031	1.203 ± 0.039	1.107 ± 0.036	1.084 ± 0.035
	(n, inl)D	1.088 ± 0.037	0.776 ± 0.027	1.113 ± 0.038	1.063 ± 0.036
	(n, inl)C	0.886 ± 0.029	0.940 ± 0.030	1.003 ± 0.032	1.021 ± 0.033
	(n, 2n)	0.902 ± 0.029	1.014 ± 0.032	0.919 ± 0.029	0.984 ± 0.031
18 cm–58°	(n, el)	0.978 ± 0.032	1.282 ± 0.042	1.187 ± 0.039	1.129 ± 0.037
	(n, inl)D	1.164 ± 0.040	0.838 ± 0.029	1.181 ± 0.041	1.082 ± 0.037
	(n, inl)C	0.862 ± 0.028	0.912 ± 0.029	0.951 ± 0.031	0.985 ± 0.032
	(n, 2n)	0.851 ± 0.027	0.959 ± 0.030	0.865 ± 0.027	0.927 ± 0.029
18 cm–73°	(n, el)	0.955 ± 0.031	1.208 ± 0.040	1.158 ± 0.038	1.055 ± 0.035
	(n, inl)D	1.042 ± 0.035	0.786 ± 0.027	1.095 ± 0.037	1.043 ± 0.035
	(n, inl)C	0.946 ± 0.030	1.004 ± 0.032	1.030 ± 0.033	1.053 ± 0.034
	(n, 2n)	0.925 ± 0.029	1.038 ± 0.033	0.942 ± 0.030	1.009 ± 0.032
18 cm–107°	(n, el)	1.288 ± 0.043	1.261 ± 0.042	1.208 ± 0.041	1.105 ± 0.037
	(n, inl)D	1.181 ± 0.041	0.900 ± 0.031	1.162 ± 0.040	1.036 ± 0.036
	(n, inl)C	0.975 ± 0.031	1.013 ± 0.032	0.973 ± 0.031	0.990 ± 0.032
	(n, 2n)	0.941 ± 0.030	1.048 ± 0.033	0.945 ± 0.030	1.021 ± 0.032
18 cm–122°	(n, el)	1.205 ± 0.040	1.120 ± 0.038	1.056 ± 0.035	0.996 ± 0.033
	(n, inl)D	1.212 ± 0.042	0.893 ± 0.031	1.148 ± 0.040	1.016 ± 0.036
	(n, inl)C	0.939 ± 0.030	0.965 ± 0.031	0.891 ± 0.029	0.918 ± 0.029
	(n, 2n)	0.897 ± 0.028	0.980 ± 0.031	0.896 ± 0.028	0.969 ± 0.031
18 cm–133°	(n, el)	1.525 ± 0.054	1.259 ± 0.045	1.197 ± 0.043	1.141 ± 0.041
	(n, inl)D	1.222 ± 0.044	0.884 ± 0.033	1.135 ± 0.041	0.997 ± 0.036
	(n, inl)C	0.931 ± 0.030	0.956 ± 0.031	0.869 ± 0.028	0.883 ± 0.028
	(n, 2n)	0.885 ± 0.028	0.958 ± 0.030	0.883 ± 0.028	0.949 ± 0.028

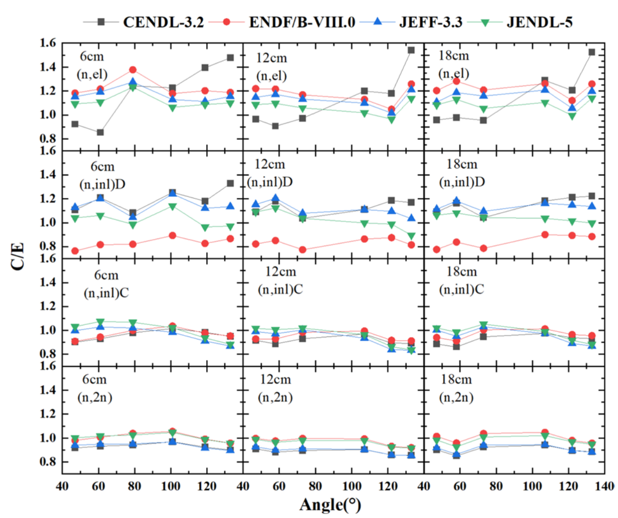

Fig. 17 (Color online) Variation in C/E values with angles

CENDL-3.2 and JENDL-5 libraries remained close to each other and exceeded 1 across all angles.

3. In the continuous energy-level inelastic scattering energy range, the C/E values of the CENDL-3.2 and ENDF/B-VIII.0 libraries exhibited a slight increasing trend with angle, whereas those of the JEFF-3.3, and JENDL-5 libraries exhibited a slight decreasing trend. At 101° and 107°, the C/E values from all the four libraries were the most similar.

4. In the (n, 2n) energy range, the C/E values of all four libraries exhibited little angular dependence. Compared with the ENDF/B-VIII.0 and JENDL-5 libraries, the C/E values from the CENDL-3.2 and JEFF-3.3 libraries were relatively lower.

4.3.4 Analysis and discussion

To further analyze the causes of the discrepancies in the C/E values observed across different databases, we employed the NDplot program to obtain secondary neutron energy spectra, double-differential cross sections, and angular distributions for various reaction channels resulting from 14.5 MeV neutrons incident on ^{nat}Zr, as illustrated in Fig. 18.

1. The angular distribution curves of the (n, el) reaction were extracted from all four libraries and compared (Fig. 18(a)). At smaller angles, the cross-sectional values from the ENDF/B-VIII.0, JENDL-5, and JEFF-3.3 libraries were significantly higher than those from the CENDL-3.2 library. However, at larger angles, the CENDL-3.2 library exhibited higher cross-sectional values than the

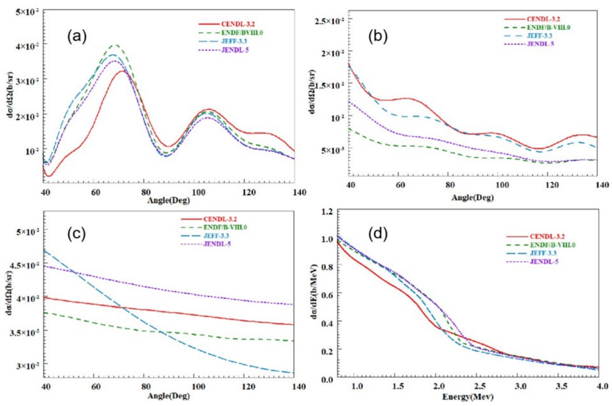

Fig. 18 (Color online) Information of secondary neutron generated by 14.5 MeV neutrons incident on ^{nat}Zr. (a) (n, el) reaction channel angular distribution. (b) (n, inl)D reaction channel angular distribution. (c) (n, inl)C reaction channel angular distribution. (d) (n, 2n) reaction channel energy spectrum

other three. This was likely the main reason why, in the elastic scattering energy range, the simulations from all libraries, except for the CENDL-3.2 library, overestimated the experimental results at small angles, and all four libraries overestimated at larger angles.

2. Figure 18(b) shows the angular distribution curves of the (n, inl)D reaction extracted from the four libraries. The (n, inl)D reaction cross section was obtained by summing the cross sections of the 40 reaction channels (MT = 51 to 90). At all angles, the cross-sectional values from the CENDL-3.2 and JEFF-3.3 libraries were relatively high, whereas those from the ENDF/B-VIII.0 library were the lowest. This likely explains why the simulation results from the CENDL-3.2 and JEFF-3.3 libraries in the discrete energy-level inelastic scattering energy range were higher than the experimental values, whereas those from the ENDF/B-VIII.0 library were lower.

3. The angular distribution curves of the (n, inl)C reaction extracted from the four libraries are shown in Fig. 18(c). The cross-sectional values of the JEFF-3.3 library decreased noticeably with increasing angle. This was likely the main reason the simulations from JEFF−3.3 library underestimated the experimental results at large angles in the continuous energy-level inelastic scattering energy range.

4. Figure 18(d) shows the (n, 2n) reaction energy spectra extracted from the four libraries. The cross-sectional values from the CENDL-3.2 and JEFF-3.3 libraries were lower than those from the ENDF/B-VIII.0 and JENDL-5 libraries. This is likely the main reason why the simulation results from the CENDL-3.2 and JEFF-3.3 libraries were lower than the experimental results in the (n, 2n) energy range.

5 Conclusion

Using the CIAE shielding integral experiment measurement system, the leakage neutron time-of-flight spectra were measured for 14.5 MeV neutrons generated by D–T fusion incident on the ^{nat}Zr slabs with thicknesses of 6, 12, and 18 cm. The measurements were performed at angles of 47°, 58° (61°), 73° (79°), 107° (101°), 122° (119°), and 133°. The MCNP program was employed to build a geometric model reflecting the experimental setup, considering the angular distribution and pulse time distribution of the source neutrons as well as the detector's efficiency. Leakage neutron spectra were calculated based on the cross-sectional data for ^{nat}Zr isotopes in CENDL-3.2, ENDF/B-VIII.0, JEFF-3.3, and JENDL-5 libraries. A comparison between the experimental and calculated results showed that the simulations from different libraries exhibited varying degrees of deviation from the measurements.

The secondary neutron energy spectrum produced by 14.5 MeV incident neutrons on ^{nat}Zr samples was obtained using the NDplot program, and the whole energy spectrum interval was divided into the elastic scattering interval (n, el), discrete energy-level inelastic scattering interval (n, inl)D, continuous energy-level inelastic scattering interval (n, inl)C, and (n, 2n) interval according to the contributions of different reaction channels to the total cross sections.

The C/E value was obtained by dividing the calculated value by the experimental value. Analyzing the C/E values for different energy regions, we obtained the following conclusions: In the (n, el) energy region, the C/E value for the CENDL-3.2 library increased with the angle. At small angles, the simulated results from CENDL-3.2 were slightly lower than the experimental values, whereas at large angles, they were significantly higher. For the other three libraries, the C/E values did not vary significantly with angle, and the simulated results were consistently higher than the experimental results. From the secondary neutron angular distribution for this reaction channel, the cross-sectional values from CENDL-3.2 library were lower than those from the other three libraries at small angles and higher at large angles. In the (n, inl)D energy region, the simulated results from CENDL-3.2 and JEFF-3.3 libraries were consistently higher than the experimental results at all angles, whereas the ENDF/B-VIII.0 library exhibited significantly lower simulation results. The cross-sectional values for ENDF/B-VIII.0 were notably lower than those of the other three libraries across all angles. In the (n, inl)C energy region, the JEFF-3.3 library simulation results were lower than the experimental values at large angles. The secondary neutron angular distribution for this reaction channel showed that the cross-sectional values from JEFF-3.3 decreased with the angle and were much lower than those from the other databases at large angles. In the (n, 2n) energy region, the simulated results from both CENDL-3.2 and JEFF-3.3 libraries were lower than the experimental results. From the secondary neutron energy spectrum of this reaction channel, the cross-sectional values for these two libraries were lower than those for the other two libraries.

These differences indicate that discrepancies still exist in the evaluated nuclear data for Zr across different libraries, particularly in the (n, el) and (n, inl)D reaction energy regions, where the differences are most pronounced. Further integral experiments are required to provide data support for improving the evaluated nuclear data of Zr.

In summary, the results of this study highlight the necessity of enhancing the accuracy and consistency of zirconium-evaluated nuclear data and provide valuable insights for improvement.

Acknowledgements The authors acknowledge all their colleagues in the accelerator operating group at CIAE for providing the excellent experimental conditions.

Author Contributions All authors contributed to the study conception and design. Material preparation, data collection, and analysis were performed by Shi-Yu Zhang, Yan-Yan Ding, and Qi Zhao. The first draft of the manuscript was written by Xin-Yi Pan, and all authors commented on previous versions of the manuscript. All authors read and approved the final manuscript.

Data Availability The data that support the findings of this study are openly available in Science Data Bank at https://cstr.cn/31253.11.sciencedb.j00186.00987 and https://www.doi.org/10.57760/sciencedb.j00186.00987.

Declarations

Conflict of interest The authors declare that they have no conflict of interest.

References

1. Z.H. Feng, C.Q. Xia, X.Y. Zhang et al., Development and application of high strength and toughness Zr alloys. Mater. Sci. Technol. **26**(2), 1–8 (2018). https://doi.org/10.11951/j.issn.1005-0299.20170022
2. X.F. Wang, Z.K. Li, J. Zhou et al., Application and research progress of Zirconium alloy in nuclear industry. Mater. Heat Treat. **41**(2), 71–74 (2012). https://doi.org/10.3969/j.issn.1001-3814.2012.02.021
3. H.G. Rickover, L.D. Geiger, B. Lustman, History of the development of zirconium alloys for use in nuclear reactors (United States Energy Research and Development Administration. Div. Naval React. (1975). https://doi.org/10.2172/4240391
4. D.O. Northwood, The development and applications of zirconium alloys. Mater. Des. **6**(2), 58–70 (1985). https://doi.org/10.1016/0261-3069(85)90165-7
5. A.T. Motta, A. Couet, R.J. Comstock, Corrosion of zirconium alloys used for nuclear fuel cladding. Ann. Rev. Mater. Res. **45**, 311–343 (2015). https://doi.org/10.1146/annurev-matsci-070214-020951
6. X.C. Ruan, Nuclear data measurement progress in China. Nucl. Tech. (in Chinese) **46**(8), 080003 (2023). https://doi.org/10.11889/j.0253-3219.2023.hjs.46.080003
7. B. Zhang, X.B. Ma, K. Hu et al., Performance of the CENDL-3.2 and other major neutron data libraries for criticality calculations. Nucl. Sci. Tech. **33**, 8 (2022). https://doi.org/10.1007/s41365-022-00994-3
8. Z.J. Liu, Y.W. Yang, L. Zheng et al., Measurement and analysis of ^{232}Th(n, 2n) reaction rate in a polyethylene shell with DT neutrons. Nucl. Tech. (in Chinese) **41**(6), 060502 (2018). https://doi.org/10.11889/j.0253-3219.2018.hjs.41.060502
9. Z.G. Ge, Y.J. Chen, Status and development of nuclear data research in China. Atom. Energy Sci. Technol. (in Chinese) **53**(10), 1742–1746 (2019). https://doi.org/10.7538/yzk.2019.53.10.1742
10. C. Ichihara, I. Kimura, J. Yamamoto et al., Measurement and analysis of leakage neutron spectrum from a spherical pile of silicon with incident 14 MeV Neutrons. J. Nucl. Sci. Technol. **44**(1), 29–35 (2007). https://doi.org/10.3327/jnst.44.29
11. D.P. Barry, G. Leinweber, R.C. Block et al., Quasi-differential neutron scattering in zirconium from 0.5 to 20 MeV. Nucl. Sci. Eng. **174**(2), 188–201 (2013). https://doi.org/10.13182/NSE12-1
12. S. Zhang, N. Song, J.C. Wang et al., Measurement of leakage neutron spectra for zirconium with D-T neutrons and validation of evaluated nuclear data. Fusion Eng. Des. **149**, 111311 (2019). https://doi.org/10.1016/j.fusengdes.2019.111311
13. L.C. Pei, X.Z. Zhang, Monte Carlo method and the application in the transport of particles. (Science Press, Beijing, 1980), pp. 100–114 (in Chinese)
14. R. Bagheri, A.K. Moghaddam, A. Yousefi, Gamma-ray shielding study of light to heavyweight concretes using MCNP-4C code. Nucl. Sci. Tech. **28**, 15 (2017). https://doi.org/10.1007/s41365-016-0167-6
15. Z.G. Ge, R.R. Xu, H.C. Wu et al., CENDL-3.2: the new version of Chinese general purpose evaluated nuclear data library. EPJ Web Conf. 239, 09001 (2020). https://doi.org/10.1051/epjconf/202023909001
16. D.A. Brown, M.B. Chadwick, R. Capote et al., ENDF/B-VIII.0: the 8th major release of the nuclear reaction data library with CIELO-project cross sections, new standards and thermal scattering data. Nucl. Data Sheets 148, 1–142 (2018). https://doi.org/10.1016/j.nds.2018.02.001
17. O. Cabellos, F. Alvarez-Velarde, M. Angelone et al., Benchmarking and validation activities within JEFF project. EPJ Web Conf. **146**, 06004 (2017). https://doi.org/10.1051/epjconf/201714606004
18. O. Iwamoto, N. Iwamoto, S. Kunieda et al., Japanese evaluated nuclear data library version 5: JENDL-5. J. Nucl. Sci. Technol. **60**(1), 1–60 (2023). https://doi.org/10.1080/00223131.2022.2141903
19. Q. Sun, Z. Chen, R. Han et al., Experiment on uranium slabs of different thicknesses with D-T neutrons and validation of evaluated nuclear data. Fusion Eng. Des. **125**, 9–17 (2017). https://doi.org/10.1016/j.fusengdes.2017.10.021
20. S. Zhang, Y.B. Nie, J. Ren et al., Benchmarking of JEFF-3.2, FENDL-3.0 and TENDL-2014 evaluated data for tungsten with 14.8MeV neutrons. Nucl. Sci. Tech. **28**, 27 (2017). https://doi.org/10.1007/s41365-017-0192-0
21. F. Luo, R. Han, Z.Q. Chen, Measurement of leakage neutron spectra from graphite cylinders irradiated with D-T neutrons for validation of evaluated nuclear data. Appl. Radiat. Isot. **116**, 185–189 (2016). https://doi.org/10.1016/j.apradiso.2016.08.009
22. S. Zhang, Z.Q. Chen, Y.B. Nie et al., Measurement of leakage neutron spectra for Tungsten with D-T neutrons and validation

of evaluated nuclear data. Fusion Eng. Des. **92**, 41–45 (2015). https://doi.org/10.1016/j.fusengdes.2015.01.010

23. Y.Y. Ding, Y.B. Nie, J. Ren et al., Benchmark experiment for bismuth by slab samples with D-T neutron source. Fusion Eng. Des. **167**, 112312 (2021). https://doi.org/10.1016/j.fusengdes.2021.112312
24. Y.B. Nie, J. Ren, X.C. Ruan et al., Benchmark experiments with slab sample using TOF technique at CIAE. Ann. Nucl. Energy **136**, 107040 (2020). https://doi.org/10.1016/j.anucene.2019.107040
25. Q. Zhao, Y.B. Nie, Y.Y. Ding et al., Measurement and simulation of the leakage neutron spectra from Fe spheres bombarded with 14MeV neutrons. Nucl. Sci. Tech. 34, 182 (2023). https://doi.org/10.1007/S41365-023-01329-6
26. H.T. Chen, F. Zhao, Establishment of microsecond pulse beam system on Cockcroft-Walton accelerator. Atom. Energy Sci. Technol. (in Chinese) **48**(7), 1300–1303 (2014). https://doi.org/10.7538/yzk.2014.48.07.1300
27. K. Zhang, Y.B. Nie, J. Bao et al., Verification of the integral experimental system with standard sample method. Nucl. Tech. (in Chinese) **37**(8), 080501 (2014). https://doi.org/10.11889/j.0253-3219.2014.hjs.37.080501
28. X.G. Cai, Y.B. Nie, J. Bao et al., Design of a pre-collimator system for neutronics benchmark experiment. Nucl. Tech. (in Chinese) **36**(1), 010201 (2013). https://doi.org/10.11889/j.0253-3219.2013.hjs.36.010201
29. N. Evans, I.R. Brearley, M.C. Scott, Neutron yield calibration of a miniature (D-T) target assembly with associated particle monitoring. Nucl. Instrum. Methods **160**(3), 465–470 (1979). https://doi.org/10.1016/0029-554X(79)90202-7
30. L. Rong, L.B. Lin, D.L. Wang, Measurement and check of fusion neutron yield with the method of associated particles at a large angle. Nucl. Electron. Detect. Technol. **19**, 428–432 (1999). https://doi.org/10.3969/j.issn.0258-0934.1999.06.006
31. Q.P. Zhong, X.J. Chen, H.L. Lu et al., Background analysis for an associated particle method to measure the neutron fluence rate from the T(d, n)^{4}He neutron source. Atom. Energy Sci. Technol. (in Chinese) **39**(2), 130–133 (2005). https://doi.org/10.7538/yzk.2005.39.02.0130
32. Y.Y. Ding, Y.B. Nie, Y. Zhang et al., Benchmark experiment on slab ^{238}U with D-T neutrons for validation of evaluated nuclear data. Nucl. Sci. Tech. **35**, 29 (2024). https://doi.org/10.1007/s41365-024-01386-5
33. H.Y. Wu, Z.H. Li, H. Tan et al., A general-purpose digital data acquisition system (GDDAQ) at Peking University. Nucl. Instrum. Methods Phys. Res. Sect. A **975**, 164200 (2020). https://doi.org/10.1016/j.nima.2020.164200
34. D. Schlegel, S. Guldbakke, Why do we need target? Paper presented at the Monte Carlo 2000 Conference. Lisbon, Portugal **23–26**, 881–886 (2000). https://doi.org/10.1007/978-3-642-18211-2_141
35. G. Dietze, H. Klein, NRESP4 and NEFF4–Monte Carlo codes for the calculation of neutron response functions and detection efficiencies for NE 213 scintillation detectors. Report by Physikalisch-Technische Bundesanstalt, Braunschweig (German, October 1982). https://ntrl.ntis.gov/NTRL/dashboard/searchResults/titleDetail/DE83750954.xhtm
36. J. Wang, X.L. Lu, Y. Yan et al., Study of an unfolding algorithm for D-T neutron energy spectra measurement using a recoil proton method. Chin. Phys. C **39**(7), 076201 (2015). https://doi.org/10.1088/1674-1137/39/7/076201
37. A. Seghour, F.Z. Seghour, Unfolding neutron energy spectra from foil fsed to produce pulsed neuactivation detector measurements with the Gold algorithm. Nucl. Instrum. Methods Phys. Res. Sect. A **457**, 617–626 (2001). https://doi.org/10.1016/S0168-9002(00)00793-2
38. Y.L. Jin, X. Tao, J.M. Wang et al., NDplot–A plotting tool for nuclear data. EPJ Web Conf. **239**, 10004 (2020). https://doi.org/10.1051/epjconf/202023910004